VIP Energy Storage Materials Very Important Paper

Deutsche Ausgabe: DOI: 10.1002/ange.201710616
Internationale Ausgabe: DOI: 10.1002/anie.201710616

MoS_2-on-MXene Heterostructures as Highly Reversible Anode Materials for Lithium-Ion Batteries

Chi Chen+, Xiuqiang Xie+, Babak Anasori, Asya Sarycheva, Taron Makaryan, Mengqiang Zhao, Patrick Urbankowski, Ling Miao, Jianjun Jiang, and Yury Gogotsi**

Abstract: *Two-dimensional (2D) heterostructured materials, combining the collective advantages of individual building blocks and synergistic properties, have spurred great interest as a new paradigm in materials science. The family of 2D transition-metal carbides and nitrides, MXenes, has emerged as an attractive platform to construct functional materials with enhanced performance for diverse applications. Here, we synthesized 2D MoS_2-on-MXene heterostructures through in situ sulfidation of $Mo_2TiC_2T_x$ MXene. The computational results show that MoS_2-on-MXene heterostructures have metallic properties. Moreover, the presence of MXene leads to enhanced Li and Li_2S adsorption during the intercalation and conversion reactions. These characteristics render the as-prepared MoS_2-on-MXene heterostructures stable Li-ion storage performance. This work paves the way to use MXene to construct 2D heterostructures for energy storage applications.*

2D heterostructures, made by stacking different 2D crystals on top of each other at the nanoscale, have properties and applications not available from their individual building blocks. Recently, 2D heterostructures including MoS_2 assembled on 2D conductive scaffolds have attracted great attention for energy storage applications.[1] MoS_2, a representative 2D transition-metal dichalcogenide, is emerging as a potential candidate for lithium-ion storage.[2] 2H MoS_2, the most common polytype, suffers from intrinsically poor electrical conductivity and large volume change upon cycling.[3] Additionally, it is documented that a polysulfide shuttling problem during the discharge process may cause premature electrode failure via electrochemical degradation of the active material.[2b] As a result, MoS_2 electrodes exhibit poor cycle stability and rate capability. However, in 2D heterostructures, the intimate interfacial interaction between MoS_2 and the conductive agent cannot only facilitate the electron transfer, but also retain the large electrode/electrolyte contact to completely fulfill the potential of the active material (MoS_2).[4] Consequently, improved electrochemical performances of MoS_2-based electrodes can be expected.

In 2011, a family of 2D materials called MXenes was discovered.[5] The formula of MXenes is $M_{n+1}X_nT_x$, where M is an early transition metal, X is carbon and/or nitrogen, $n=1, 2$ or 3, and T_x refers to surface terminations such as OH, O and F.[6] Due to their layered structure and high conductivity, MXenes are well-suited for energy storage.[7] In particular, MXenes are promising candidates for lithium-ion storage.[8] On one hand, the low Li^+ diffusion barriers on the MXenes' surface[8a] and their excellent conductivity[9] could facilitate ionic and electronic transport. On the other hand, MXenes have been applied to confine different materials and prevent their cracking during charge-discharge cycling, incld/ inclduing metal oxides, polymers, and MoS_2.[10] However, MXene-based 2D/2D heterostructures have not reported so far.

In 2015, we discovered an ordered double transition-metal $Mo_2TiC_2T_x$ MXene, in which an atomic layer of Ti is sandwiched between two layers of Mo in the metal carbide structure. This unique arrangement of atoms gives $Mo_2TiC_2T_x$ different properties than the $Ti_3C_2T_x$ MXene.[11] Since only Mo atoms are on the surface of $Mo_2TiC_2T_x$ MXenes, its surface Mo−O motifs might be converted into Mo−S bonds under a certain condition, resulting in the formation of MoS_2, similar to the transformation from MoO_2 or MoO_3 to MoS_2.[12] Here, we prepared few-layered MoS_2 on $Mo_2TiC_2T_x$ MXene heterostructures by an in situ sulfidation method. The 2D MoS_2-on-MXene heterostructures feature intimate interfacial interactions, which maximize the potential of conductive MXene as support for MoS_2.

$MoS_2/Mo_2TiC_2T_x$ heterostructures were prepared as schematically illustrated in Figure 1a. (Experimental details are provided in the Supporting Information.) In the first step, $Mo_2TiC_2T_x$ with sulfur particles incorporated between the MXene flakes ($S/Mo_2TiC_2T_x$) were obtained by a liquid mixing process. We hypothesized that heating $S/Mo_2TiC_2T_x$ hybrids in an inert atmosphere could transform Mo−O motifs to MoS_2 on the surface of $Mo_2TiC_2T_x$ and remove residual sulfur simultaneously, producing $MoS_2/Mo_2TiC_2T_x$ heterostructures. To do so, we heat treated the $S/Mo_2TiC_2T_x$ hybrids at 500 °C or 700 °C for 4 hours under argon, and the as-obtained products were denoted as $MoS_2/Mo_2TiC_2T_x$-500 and $MoS_2/Mo_2TiC_2T_x$-700, respectively.

In the Raman spectrum of pure $Mo_2TiC_2T_x$ (Figure 1b), we can ascribe the band at $164\ cm^{-1}$ to E_g vibrations from both Mo and Ti atoms in the oxygen-terminated Mo_2TiC_2.

---

[*] C. Chen,[+] Dr. X. Q. Xie,[+] Prof. B. Anasori, A. Sarycheva,
Dr. T. Makaryan, Dr. M. Q. Zhao, P. Urbankowski, Prof. Y. Gogotsi
A.J. Drexel Nanomaterials Institute
Materials Science and Engineering Department
Drexel University, 3141 Chestnut Street
Philadelphia, PA 19104 (USA)
E-mail: gogotsi@drexel.edu
C. Chen,[+] Prof. L. Miao, Prof. J. J. Jiang
School of Optical and Electronic Information
Huazhong University of Science and Technology
Wuhan, Hubei 430074 (P. R. China)
E-mail: miaoling@mail.hust.edu.cn

[+] These authors contributed equally to this work.

Supporting information and the ORCID identification number(s) for the author(s) of this article can be found under: https://doi.org/10.1002/anie.201710616.

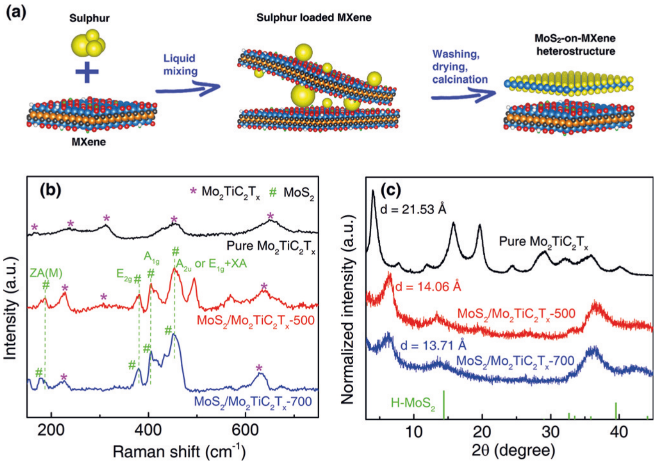

Figure 1. a) Schematic illustration of the preparation of MoS_2/MXene hybrids. S/$Mo_2TiC_2T_x$ hybrids were obtained by a liquid mixing process (left panel). Then the sulfur loaded MXene (middle panel) was head treated to obtain MoS_2-on-MXene heterostructures (right panel). b) Raman spectra and c) XRD patterns of pure $Mo_2TiC_2T_x$, MoS_2/$Mo_2TiC_2T_x$-500 and MoS_2/$Mo_2TiC_2T_x$-700.

The O-termination itself contributes mostly as an E_g vibration at 234 cm^{-1}. Higher frequencies (311, 450 and 650 cm^{-1}) can be attributed to mostly C vibrations in $Mo_2TiC_2O_2$.[13] In the Raman spectrum of MoS_2/$Mo_2TiC_2T_x$-500, two bands at 381 and 404 cm^{-1} are observed, which are assigned to the in-plane E_{2g} and out-of-plane A_{1g} modes of 2H-phased MoS_2, respectively.[14] The band at around 570 cm^{-1} could be attributed to $2E_{1g}$[15] or $A_{2u}+XA$ vibrations.[15b] Moreover, since the 633 nm excitation is in resonance with the indirect band gap of MoS_2, one-phonon-forbidden Raman vibrations can now be seen at 454 cm^{-1}, which can be attributed to A_{2u} or $E_{1g}+XA$ band. The vibration at 187 cm^{-1} can be attributed to the acoustic out-of-plane mode ZA(M).[16] These vibrations could also be observed for MoS_2/$Mo_2TiC_2T_x$-700, indicating the formation of MoS_2. The formation of MoS_2 could also be verified by high-resolution X-ray photoelectron spectroscopy. (Details are provided in Supporting Information and Figure S1.)

The XRD pattern of the pure $Mo_2TiC_2T_x$ (Figure 1c) shows only the (*00l*) peaks with *d*-spacing of 21.53 Å. The appearance of all the (*00l*) peaks indicates the strong restacking of the flakes in the filtered MXene film.[11b] The *d*-spacing of $Mo_2TiC_2T_x$ decreased from 21.53 Å to 14.06 and 13.71 Å for MoS_2/$Mo_2TiC_2T_x$-500, and MoS_2/$Mo_2TiC_2T_x$-700, respectively. The peak around 13.5° in the XRD patterns of the heat-treated samples can correspond to both the (004) peak of $Mo_2TiC_2T_x$ and the (002) peak of MoS_2 with *d*-spacing of 6.62 Å. Additionally, new peaks appeared in the XRD patterns of the heat-treated samples: two broad peaks at 36 and 43° and a narrower peak at 63° (Figures 1c and Figure S2), matching the peaks of 2H MoS_2, with smaller *a*-lattice parameter (*a*-LP). These peaks were shifted to the left as we increased the time and temperature of the heat-treatment. The reported *a*-LP of $Mo_2TiC_2T_x$ at 2.93 Å is smaller than that of the MoS_2 at 3.16 Å,[11b,17] resulting in lattice mismatch while forming heterostructures. With increasing heat-treatment time and temperature, more MoS_2 forms on $Mo_2TiC_2T_x$, reducing the mismatch effect and enhancing the interaction between the MoS_2 layers. (Details are provided in Supporting Information and Figure S2.)

The scanning electron microscopy (SEM) images of MoS_2/$Mo_2TiC_2T_x$-500 and MoS_2/$Mo_2TiC_2T_x$-700 are shown in Figure 2a and b. Compared to pure $Mo_2TiC_2T_x$ fabricated by filtration of a stable colloidal solution, which is composed of well-aligned stacked 2D sheets,[11a] the MoS_2/$Mo_2TiC_2T_x$ heterostructures are disordered and have an open architecture constructed of 2D sheets. From energy-dispersive X-ray spectrometry (Tables S1 and S2), the atomic content of S increased with the temperature, and the Mo:S ratio was 2:0.95 and 2:2.09 for MoS_2/$Mo_2TiC_2T_x$-500 and MoS_2/$Mo_2TiC_2T_x$-700, respectively. Accordingly, the $Mo_2TiC_2T_x$:MoS_2 ratios are calculated to be 1:0.62 and 1:2.19 for MoS_2/$Mo_2TiC_2T_x$-500 and MoS_2/$Mo_2TiC_2T_x$-700, respectively. The transmission electron microscopy (TEM) images of MoS_2/$Mo_2TiC_2T_x$-500 are shown in Figure 2c. A lattice spacing of about 14.0 Å was identified, which is in agreement with the (002) peak position in the XRD pattern of the $Mo_2TiC_2T_x$. In addition, a newly formed layered compound on $Mo_2TiC_2T_x$ with an interlayer spacing of 6.9 Å was found, similar to that of bulk MoS_2 (6.15 Å).[18] This value is in agreement with the *d*-spacing that we calculated from the (002) peak of MoS_2 in XRD patterns. Figure 2c shows that two layers of MoS_2 contact intimately with $Mo_2TiC_2T_x$ layers, forming MoS_2-on-MXene heterostructures. From the TEM image of MoS_2/$Mo_2TiC_2T_x$-700 (Figure 2d), it can be seen that there are more MoS_2 layers, suggesting that a higher temperature of 700 °C facilitates the formation of MoS_2.

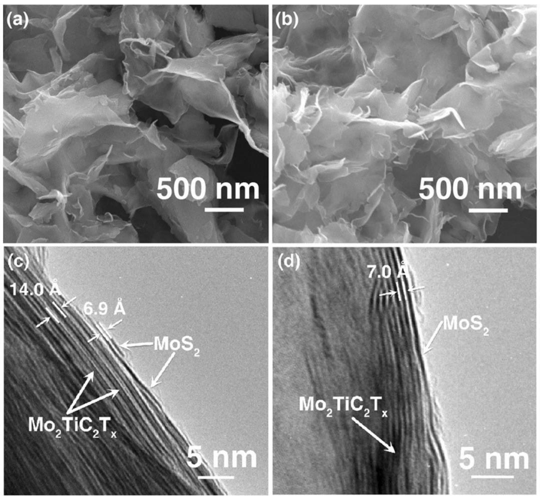

Figure 2. SEM images of a) MoS_2/$Mo_2TiC_2T_x$-500 and b) MoS_2/$Mo_2TiC_2T_x$-700. Cross-sectional TEM images of MoS_2-on-MXene heterostructures: c) MoS_2/$Mo_2TiC_2T_x$-500 and d) MoS_2/$Mo_2TiC_2T_x$-700.

We also performed computational investigations of the structural and electronic properties of the heterostructure. (Computational details are provided in the Supporting Information and detailed results are shown in Figure S3.) Our calculated *a*-LP for MoS_2 and MoS_2/$Mo_2TiC_2O_2$ are 3.16 and 3.06 Å, respectively, in agreement with the XRD data.

Figure S3b shows the band structures of the MoS_2, $Mo_2TiC_2O_2$ and $MoS_2/Mo_2TiC_2O_2$ hybrid. Pure MoS_2 is a semiconductor with a direct band gap of 1.7 eV, while $Mo_2TiC_2O_2$ shows metallic properties, which agrees with previous results.[11b] The hybrid $MoS_2/Mo_2TiC_2O_2$ structure also shows metallic properties. It suggests that the integration between MoS_2 and $Mo_2TiC_2O_2$ can significantly improve the conductivity of the MoS_2, which is desirable for high-rate charging/discharging.

The lithium storage performance of the as-obtained $MoS_2/Mo_2TiC_2T_x$ heterostructures was evaluated in lithium-ion half-cells. The cyclic voltammetry (CV) curves of pure $Mo_2TiC_2T_x$ are shown in Figure S4, indicating a capacitor-like performance without obvious redox peaks. Figure 3a shows the CV curves of $MoS_2/Mo_2TiC_2T_x$-500. In the first cycle, the cathodic peak at 0.8 V represents the intercalation of lithium ions into the triangular prism structure of MoS_2 or $Mo_2TiC_2T_x$, while the peak at 0.5 V could be the reduction of Li_xMoS_2 to Mo and Li_2S based on the conversion reaction.[2b,19] Another small cathodic peak around 0.2 V could be due to the formation of a solid electrolyte interface (SEI) layer or an irreversible reactions of Li with the surface functional groups. In the anodic scan, the peak at 1.3 V could be assigned to the oxidation of Mo and delithiation of $Li_xMo_2TiC_2T_x$, while the peak at 2.3 V could be corresponded to the delithiation of Li_2S.[2b,11a] In the subsequent cathodic scan, the peaks at 1.2 and 1.9 V could be assigned to the formation of Li_xMoS_2 and Li_2S, respectively.[2] Analogous cathodic and anodic peaks could be observed in CV curves for $MoS_2/Mo_2TiC_2T_x$-700 (Figure S5). These reactions also can be found from galvanostatic charge/discharge curves (Figure 3c). In discharge processes, the plateaus around 1.9 and 1.2 V indicate the formation of Li_2S and Li_xMoS_2, while the plateaus at around 1.3 and 2.3 V in charge processes coming from the oxidation of Mo or delithiation of $Li_xMo_2TiC_2T_x$, and the delithiation of Li_2S.

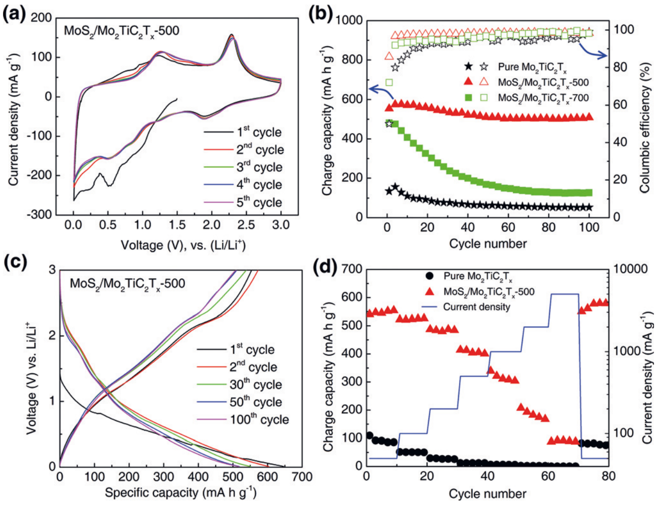

Figure 3. Electrochemical performance of $MoS_2/Mo_2TiC_2T_x$ heterostructures for lithium-ion batteries. a) CV curves of $MoS_2/Mo_2TiC_2T_x$-500 at 1 mV s^{-1}, b) cycling stabilities and Coulombic efficiencies for pristine $Mo_2TiC_2T_x$, $MoS_2/Mo_2TiC_2T_x$-500 and $MoS_2/Mo_2TiC_2T_x$-700 at 100 mA g^{-1}, c) galvanostatic charge/discharge curves of $MoS_2/Mo_2TiC_2T_x$-500 at 100 mA g^{-1}, d) rate performance for pristine $Mo_2TiC_2T_x$ and $MoS_2/Mo_2TiC_2T_x$-500.

As shown in Figure 3b, at 100 mA g^{-1}, $MoS_2/Mo_2TiC_2T_x$-500 delivered initial charge and discharge capacities of 554 and 646 mA h g^{-1}, which are 4.1 and 2.4 times of those of pure $Mo_2TiC_2T_x$ (134 and 268 mA h g^{-1}, respectively). The obtained charge capacity is also much higher than multilayer $Mo_2TiC_2T_x$ reported previously.[11a] The enhanced capacity could be attributed to an open structure of $MoS_2/Mo_2TiC_2T_x$ compared to the restacked pure $Mo_2TiC_2T_x$, leading to smaller ion diffusion resistance as shown in the electrochemical impedance spectra (Figure S6), as well as much higher theoretical capacity of 670 mA h g^{-1} of MoS_2.[20] In addition, the initial Coulombic efficiency of $MoS_2/Mo_2TiC_2T_x$-500 is 86 %, which is much higher than that of pure $Mo_2TiC_2T_x$ (50 %). In the following cycles, the charge capacity of $MoS_2/Mo_2TiC_2T_x$-500 increases to 580 mA h g^{-1}, due to the activation of the electrode material. After 100 cycles, the charge capacity remains at 509 mA h g^{-1}, which is 92 % of its first cycle and 9.7 times of the capacity obtained by pure $Mo_2TiC_2T_x$ (52 mA h g^{-1}), demonstrating good cycling performance. The good cycling stability can also be observed in charge-discharge curves as shown in Figure 3c. Compared with pure MoS_2,[21] $MoS_2/Mo_2TiC_2T_x$-500 hybrid also shows enhanced capacity and cycling performance. On the other hand, $MoS_2/Mo_2TiC_2T_x$-700 exhibits a charge capacity of 482 mA h g^{-1} in the first cycle but a poor cycling performance and decreases to 126 mA h g^{-1} after 100 cycles (Figure 3b). This could be ascribed to the formation of a large amount of MoS_2 in $MoS_2/Mo_2TiC_2T_x$-700 as discussed above. Moreover, the Coulombic efficiencies follow the order of $MoS_2/Mo_2TiC_2T_x$-500 > $MoS_2/Mo_2TiC_2T_x$-700.

Figure 3d shows the rate performances of pure $Mo_2TiC_2T_x$ and $MoS_2/Mo_2TiC_2T_x$-500. At a current density of 50 mA g^{-1}, a high reversible average capacity of 548 mA h g^{-1} can be achieved. As the current density gradually changed to 100, 200, 500, 1000 and 2000 mA g^{-1}, the $MoS_2/Mo_2TiC_2T_x$-500 electrode delivered capacities of 523, 484, 407, 315 and 182 mA h g^{-1}, respectively. Even at a high rate of 5000 mA g^{-1}, $MoS_2/Mo_2TiC_2T_x$-500 had the capacity of 90 mA h g^{-1}. When the current density returned to 50 mA g^{-1}, the capacity returned to 572 mA h g^{-1}. For pure $Mo_2TiC_2T_x$, the average capacities at all scan rates were below 100 mA g^{-1} and decreased further with the increasing scan rate. Compared with pure MoS_2,[21] $MoS_2/Mo_2TiC_2T_x$-500 hybrid also shows enhanced rate performance.

It is well-known that pure MoS_2 electrodes suffer from poor cycling performance.[21] To investigate the reason for our enhanced lithium storage performance, we performed first-principles calculations to study the influence of $Mo_2TiC_2T_x$ MXene on the adsorption behavior of Li and its discharge product Li_2S. In the Li intercalation step, three Li adsorption sites are considered on MoS_2 and $MoS_2/Mo_2TiC_2O_2$ surfaces, as shown in Figure 4a and b. For these sites, the $MoS_2/Mo_2TiC_2O_2$ shows stronger Li adsorption with lower binding energies (Figure 4c). For both $MoS_2/Mo_2TiC_2O_2$ and MoS_2, Li prefers to stay on top of Mo (site I). As shown in Figure 4d and e, electrons will transfer from Li to $MoS_2/Mo_2TiC_2O_2$ or MoS_2. Different from pure MoS_2, the oxygen surface in the

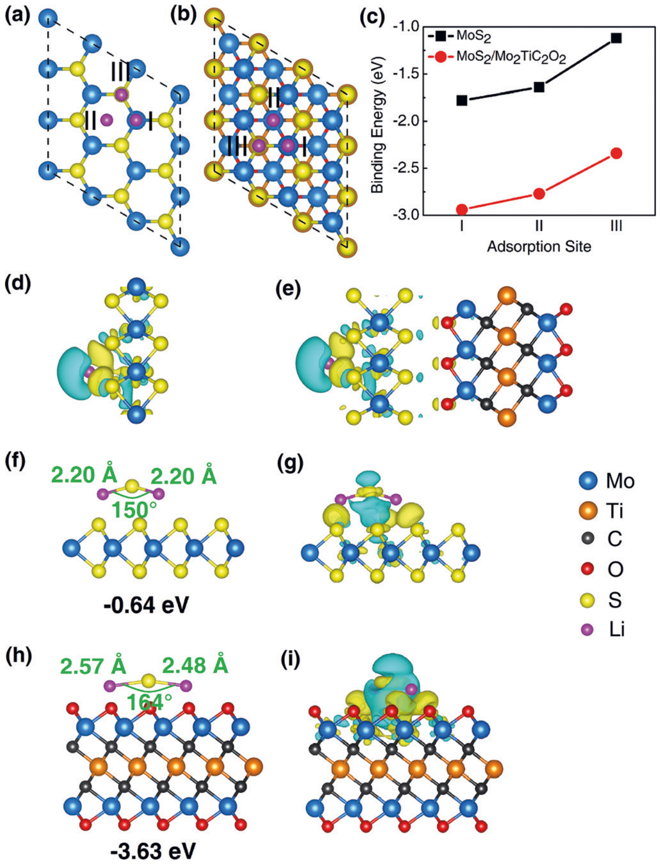

Figure 4. Adsorption sites for Li on a) MoS_2 and b) $MoS_2/Mo_2TiC_2O_2$. c) Binding energies of Li on the surface of MoS_2 and $MoS_2/Mo_2TiC_2O_2$. Differences of charge density for Li on d) MoS_2 and e) $MoS_2/Mo_2TiC_2O_2$. The most stable adsorption configurations and binding energies of Li_2S on f) MoS_2 and h) $Mo_2TiC_2O_2$. Differences in charge density of Li_2S on g) MoS_2 and i) $Mo_2TiC_2O_2$. Turquoise and yellow regions show the depletion and accumulation of electrons, respectively.

$MoS_2/Mo_2TiC_2O_2$ interface also shows electrons accumulation, indicating stronger charge transfer.

In the following step, Li_xMoS_2 will convert into Li_2S in the cathodic process and the reversible reaction will occur in the anodic process. Therefore, an effective host for the intermediate Li_2S will be important for a high Coulombic efficiency and stable cycling performance. Three relaxed adsorption configurations and corresponding binding energies of Li_2S on MoS_2 and $Mo_2TiC_2O_2$ surfaces are presented in Figure 4 f, h and S6. Apparently, $Mo_2TiC_2O_2$ shows a stronger adsorption for Li_2S with lower binding energies. The structure of the Li_2S molecule is shown in Figure S7 with Li-S bond length of 2.09 Å and Li-S-Li bond angle of 138°. Compared with Li_2S adsorption on MoS_2 as shown in Figure 4 f, $Mo_2TiC_2O_2$ will lead to larger transformation of Li_2S in bond length and angle shown in Figure 4 h, implying stronger interaction between Li_2S and $Mo_2TiC_2O_2$. As shown in Figure 4 g and i, more obvious charge transfer between Li_2S and $Mo_2TiC_2O_2$ implies a stronger interaction.

In fact, during the conversion from Li_xMoS_2 to Li_2S, several intermediate polysulfides will form.[22] Similar to Li-sulfur batteries, the polysulfide shuttling problem during discharge process may also occur.[2b] Here, we took Li_2S_2 as an example to investigate the adsorption of intermediates on MoS_2 and $Mo_2TiC_2O_2$ surfaces as shown in Figure S8. $Mo_2TiC_2O_2$ also shows more stable adsorption for Li_2S_2 with lower binding energy and larger electron transfer. The computational analysis suggests the stronger adsorption of Li, Li_2S and related intermediates, and it contributes to the enhanced lithium storage performance of the $MoS_2/Mo_2TiC_2O_2$ hybrid. The synergies between $Mo_2TiC_2O_2$ and MoS_2 lead to improved capacity, Coulombic efficiency and stable cycling performance, which could explain the enhanced performance of MoS_2-on-MXene heterostructures.

In summary, heterostructures with few layers of MoS_2 contacting intimately with $Mo_2TiC_2T_x$ MXene layers, MoS_2-on-MXene, were obtained by an in situ sulfidation of $Mo_2TiC_2T_x$ MXene. First-principles calculations predict that the heterostructures are metallic because of the presence of the highly conductive MXene. When used as anode materials for lithium-ion batteries, the as-prepared MoS_2-on-MXene heterostructures exhibited high specific capacities and Coulombic efficiencies, promising rate capability, and excellent cycling stability. The computational results reveal that the strong Li adsorption on 2D MoS_2-on-MXene heterostructures leads to its enhanced intercalation, and stable lithium polysulfide adsorption contributes to improved Coulombic efficiency and cycling performance. Our work demonstrates a possibility of constructing MXene-based 2D heterostructures for use as electrode materials for energy storage and conversion, as well as other applications.

Acknowledgements

This work was supported by the Fluid Interface Reactions, Structures, and Transport (FIRST) Center, an Energy Frontier Research Center funded by the U.S. Department of Energy, Office of Science, Basic Energy Sciences. Chi Chen was supported by the Chinese Scholarship Council (CSC). The authors thank the Core Research Facilities of Drexel University for providing access to SEM, XPS, XRD, and TEM. The computational resources were provided by Intelligent Electronics Institute, Huazhong University of Science and Technology, China.

Conflict of interest

The authors declare no conflict of interest.

Keywords: density functional theory · heterostructures · lithium-ion batteries · molybdenum disulfide · MXenes

How to cite: *Angew. Chem. Int. Ed.* **2018**, *57*, 1846–1850
Angew. Chem. **2018**, *130*, 1864–1868

---

[1] E. Pomerantseva, Y. Gogotsi, *Nat. Energy* **2017**, *2*, 17089.
[2] a) T. Stephenson, Z. Li, B. Olsen, D. Mitlin, *Energy Environ. Sci.* **2014**, *7*, 209–231; b) H. Jiang, D. Ren, H. Wang, Y. Hu, S. Guo,

H. Yuan, P. Hu, L. Zhang, C. Li, *Adv. Mater.* **2015**, *27*, 3687 – 3695.

[3] Y. M. Chen, X. Y. Yu, Z. Li, U. Paik, X. W. D. Lou, *Sci. Adv.* **2016**, *2*, e1600021.

[4] a) Y. Jing, E. O. Ortiz-Quiles, C. R. Cabrera, Z. Chen, Z. Zhou, *Electrochim. Acta* **2014**, *147*, 392 – 400; b) Y. Jing, Z. Zhou, C. R. Cabrera, Z. Chen, *J. Mater. Chem. A* **2014**, *2*, 12104 – 12122; c) C. Tan, H. Zhang, *Chem. Soc. Rev.* **2015**, *44*, 2713 – 2731; d) X. Zhang, Z. Lai, C. Tan, H. Zhang, *Angew. Chem. Int. Ed.* **2016**, *55*, 8816 – 8838; *Angew. Chem.* **2016**, *128*, 8960 – 8984; e) X. Cao, Y. Shi, W. Shi, X. Rui, Q. Yan, J. Kong, H. Zhang, *Small* **2013**, *9*, 3433 – 3438.

[5] M. Naguib, M. Kurtoglu, V. Presser, J. Lu, J. Niu, M. Heon, L. Hultman, Y. Gogotsi, M. W. Barsoum, *Adv. Mater.* **2011**, *23*, 4248 – 4253.

[6] a) M. Naguib, V. N. Mochalin, M. W. Barsoum, Y. Gogotsi, *Adv. Mater.* **2014**, *26*, 992 – 1005.

[7] a) M. Ghidiu, M. R. Lukatskaya, M. Q. Zhao, Y. Gogotsi, M. W. Barsoum, *Nature* **2014**, *516*, 78 – 81; b) B. Anasori, M. R. Lukatskaya, Y. Gogotsi, *Nat. Rev. Mater.* **2017**, *2*, 16098; c) J.-C. Lei, X. Zhang, Z. Zhou, *Front. Phys.* **2015**, *10*, 276 – 286; d) X. Zhang, Z. Zhang, Z. Zhou, *J. Energy Chem.* **2018**, *27*, 73 – 85; e) H. Zhang, *ACS Nano* **2015**, *9*, 9451 – 9469.

[8] a) Q. Tang, Z. Zhou, P. Shen, *J. Am. Chem. Soc.* **2012**, *134*, 16909 – 16916; b) M. Naguib, J. Halim, J. Lu, K. M. Cook, L. Hultman, Y. Gogotsi, M. W. Barsoum, *J. Am. Chem. Soc.* **2013**, *135*, 15966 – 15969.

[9] Z. Ling, C. E. Rena, M.-Q. Zhao, J. Yang, J. M. Giammarco, J. Qiu, M. W. Barsoum, Y. Gogotsi, *Proc. Natl. Acad. Sci. USA* **2014**, *111*, 16676 – 16681.

[10] a) M.-Q. Zhao, M. Torelli, C. E. Ren, M. Ghidiu, Z. Ling, B. Anasori, M. W. Barsoum, Y. Gogotsi, *Nano Energy* **2016**, *30*, 603 – 613; b) C. Chen, M. Boota, X. Xie, M. Zhao, B. Anasori, C. E. Ren, L. Miao, J. Jiang, Y. Gogotsi, *J. Mater. Chem. A* **2017**, *5*, 5260 – 5265; c) X. Wu, Z. Wang, M. Yu, L. Xiu, J. Qiu, *Adv. Mater.* **2017**, *29*, 1607017.

[11] a) B. Anasori, Y. Xie, M. Beidaghi, J. Lu, B. C. Hosler, L. Hultman, P. R. C. Kent, Y. Gogotsi, M. W. Barsoum, *ACS Nano* **2015**, *9*, 9507 – 9516; b) B. Anasori, C. Shi, E. J. Moon, Y. Xie, C. A. Voigt, P. R. C. Kent, S. J. May, S. J. L. Billinge, M. W. Barsoum, Y. Gogotsi, *Nanoscale Horiz.* **2016**, *1*, 227 – 234.

[12] a) D. Zhu, H. Shu, F. Jiang, D. Lv, V. Asokan, O. Omar, J. Yuan, Z. Zhang, C. Jin, *npj 2D Mater. Appl.* **2017**, *1*, 8; b) Y. C. Lin, W. Zhang, J. K. Huang, K. K. Liu, Y. H. Lee, C. T. Liang, C. W. Chu, L. J. Li, *Nanoscale* **2012**, *4*, 6637 – 6641.

[13] L. Li, *Comp. Mater. Sci.* **2016**, *124*, 8 – 14.

[14] H. Li, Q. Zhang, C. C. R. Yap, B. K. Tay, T. H. T. Edwin, A. Olivier, D. Baillargeat, *Adv. Funct. Mater.* **2012**, *22*, 1385 – 1390.

[15] a) B. Chakraborty, H. S. S. R. Matte, A. K. Sood, C. N. R. Rao, *J. Raman Spectrosc.* **2013**, *44*, 92 – 96; b) K. Gołasa, M. Grzeszczyk, R. Bożek, P. Leszczyński, A. Wysmołek, M. Potemski, A. Babiński, *Solid State Commun.* **2014**, *197*, 53 – 56.

[16] M. Placidi, M. Dimitrievska, V. Izquierdo-Roca, X. Fontané, A. Castellanos-Gomez, A. Pérez-Tomás, N. Mestres, M. Espindola-Rodriguez, S. López-Marino, M. Neuschitzer, V. Bermudez, A. Yaremko, A. Pérez-Rodríguez, *2D Mater.* **2015**, *2*, 035006.

[17] T. Böker, R. Severin, A. Müller, C. Janowitz, R. Manzke, D. Voß, P. Krüger, A. Mazur, J. Pollmann, *Phys. Rev. B* **2001**, *64*, 235305.

[18] N. Wakabayashi, H. G. Smith, R. M. Nicklow, *Phys. Rev. B* **1975**, *12*, 659 – 663.

[19] Y. Chao, R. Jalili, Y. Ge, C. Wang, T. Zheng, K. Shu, G. G. Wallace, *Adv. Funct. Mater.* **2017**, *27*, 1700234.

[20] X. Xiong, W. Luo, X. Hu, C. Chen, L. Qie, D. Hou, Y. Huang, *Sci. Rep.* **2015**, *5*, 9254.

[21] Y. Zhang, Y. Wang, J. Yang, W. Shi, H. Yang, W. Huang, X. Dong, *2D Mater.* **2016**, *3*, 024001.

[22] L. Oakes, R. Carter, T. Hanken, A. P. Cohn, K. Share, B. Schmidt, C. L. Pint, *Nat. Commun.* **2016**, *7*, 11796.

Manuscript received: October 22, 2017
Revised manuscript received: December 28, 2017
Accepted manuscript online: January 2, 2018
Version of record online: January 17, 2018